OPEN ACCESS

University of BRISTOL

Terkovics, N., Neild, S. A., Lowenberg, M. H., & Krauskopf, B. (2014). Bifurcation Analysis of a Coupled Nose Landing Gear-Fuselage System. *Journal of Aircraft*, *51*(1), 259-272. https://doi.org/10.2514/1.C032324

Peer reviewed version

License (if available):
CC BY-NC

Link to published version (if available):
10.2514/1.C032324

Link to publication record in Explore Bristol Research
PDF-document

University of Bristol - Explore Bristol Research
General rights

This document is made available in accordance with publisher policies. Please cite only the published version using the reference above. Full terms of use are available:
http://www.bristol.ac.uk/red/research-policy/pure/user-guides/ebr-terms/

Bifurcation Analysis of a Coupled Nose Landing Gear-Fuselage System

Nándor Terkovics*, Simon Neild†, Mark Lowenberg‡
University of Bristol, Bristol, BS8 1TR, UK
Bernd Krauskopf§
University of Auckland, Auckland, 1142, New Zealand

Under certain conditions during take-off and landing, pilots may sometimes experience vibrations in the cockpit. Since the cockpit is located right above the nose landing gear – which is known to potentially be prone to self-excited vibrations at certain velocities – an explanation for those vibrations might be oscillations of the landing gear feeding into the fuselage. However, the fuselage dynamics itself may also influence the dynamics of the landing gear, meaning that the coupling must be considered as bi-directional. A mathematical model is developed to study a coupled nose landing gear-fuselage system, which allows to assess the overall influence of the coupling on the system dynamics. Bifurcation analysis reveals that this interaction may be significant in both directions, and that the system behaviour depends strongly on the modal characteristics of the fuselage.

I. Introduction

At the design and testing stage of an aircraft, vibrations during take-off and landing, especially in the cockpit, must be considered to ensure that they remain small. A potential source of such oscillations is via the dynamic interaction between the fuselage rigid-body and/or flexible modes and the nose landing gear system when the aircraft is in motion on the ground.

*PhD Student, Department of Mechanical Engineering and AIAA Student Member
†Reader in Dynamics and Control, Department of Mechanical Engineering
‡Reader in Flight Dynamics, Department of Aerospace Engineering
§Professor of Applied Mathematics, Department of Mathematics, Faculty of Science

It is well known that wheeled vehicles can experience self-excited wheel vibrations under certain conditions. The phenomenon, referred to as shimmy, has interested researchers since the late 1940s when von Schlippe and Dietrich[1] published the first results on the dynamics of elastic tyres and gave the first explanation for shimmy by the so called "stretched string tyre model". In that model the tyre-ground interface is considered as a contact line that becomes deformed due to the lateral displacement of the tyre; the contact line is modeled as a straight line between the leading and trailing points. Pacejka[2–4] extended the stretched string tyre model by approximating the contact line with various stationary shape functions, and incorporated it into various vehicle models. He showed both theoretically and experimentally that periodic and quasi-periodic shimmy oscillations may occur in flexible wheeled structures. As another approach, the"exact stretched string tyre model" of Segel[5] models the contact line without any restrictions to the shape and so considers the actual and dynamically varying shape of the contact region. Stépán[6] used the exact stretched string tyre model and studied a single degree-of-freedom pulled trailer by means of nonlinear techniques. In that study the mathematical model is given as a coupled partial differential – integro-differential equation system, where the partial differential part has a travelling wave-like solution, which introduces time delay into the system. This model was further extended and experimentally tested by Takács et al.[7,8]

A nose landing gear (referred to as NLG), fitted with an elastic tyre and having structural flexibilities, can also experience shimmy oscillations, and these have been of interest since aircrafts exist. Smiley[9] used linear techniques to study three different landing gear configurations and to correlate different tyre models. More recently Somieski[10] introduced nonlinearities into the existing landing gear models and found supercritical Hopf bifurcations and stable limit cycles and, hence, gave an explanation for the onset of shimmy. Recent results on the topic were published by Thota et al.[11,12] In those studies, not only is a non-zero rake angle considered, but also a lateral degree-of-freedom is introduced to the landing gear model; the torsional and lateral degrees-of-freedom are coupled via the lateral deformation of the tyre. The body of the aircraft is considered as a block of mass that exerts a fixed vertical force F_z on the gear while the aircraft is moving at a forward velocity V.[11,12] This approach allows one to determine the occurrence of (different types of) shimmy oscillations in the (V, F_z)-plane. The analysis showed that, beyond stable torsional shimmy oscillations, stable lateral vibrations can also be triggered. Furthermore, a large region of bistability, where both types of shimmy oscillations are possible, was found, as well as quasi-periodic shimmy oscillations.[11,12] The term shimmy, which historically only referred to the torsional vibrations of wheels and wheeled structures, is, therefore, used here to describe more general mechanical vibrations in aircraft landing gears or other tyred systems.

During ground manoeuvres the aircraft is supported by the landing gears. Therefore,

oscillations of the landing gears are potential sources of excitation for the aircraft body. In particular, the oscillation of the NLG, which is attached to the fuselage and located right below the cockpit may feed directly into the fuselage and excite vibrations in the cockpit. On the other hand, an oscillating aircraft body can also influence the behaviour of the NLG. In order to clarify this mutual interaction, a coupled NLG-fuselage system is developed and analysed here.

A second motivation for the coupling is the wish to evaluate the feasibilty of the application of real-timedynamic substructuring (RTDS)[13,14] to the NLG-fuselage system. Real-time dynamic substructuring is an effective way of testing complicated systems, where complete numerical modelling or experimental testing is difficult. In an RTDS-test, a part of the physical system is experimentally tested and the remainder is modelled numerically. Advanced real-time control techniques are used to effectively 'glue together' the test specimen and the numerical model of the remainder of the system, via a transfer system (ie. actuators). Through displacement control of the actuators and force feedback to the numerical model the physical-numerical interface can be matched, so that the dynamics of the overall system is replicated.[13,14] A natural choice for the test component in the present context is the entire nose landing gear, which is coupled to a numerical model of the fuselage. However, for an RTDS-test to be reasonable, sufficient force or displacement feedback is essential. In our case this means significant interaction between the fuselage and the landing gear. Therefore, in order to study the feasibilty of an RTDS-test on a landing gear-fuselage system, not only do we need to examine the interaction itself, but we also have to study when it is significant to provide sufficient feedback.

The coupled model considers the same landing gear configuration as that of [12]. However, beside being coupled via the tyre only, the landing gear modes here considered are coupled directly as well via the geometry of the strucure. Part of this extended NLG model is the dynamic model of the fuselage, which is – for simplicity – represented by a second-order linear mass-spring-damper unit (referred to as *MSD*) attached to the top of the landing gear strut. The MSD is characterized by its natural frequency, relative damping and an effective (modal) mass. Further, the effective fuselage weight acting on the NLG, when the system is in equlibrium, and the weight of the NLG are represented by static, vertical forces. The exact stretched string tyre model completes the system; however, only the leading point of the contact region is considered to calculate the tyre force and, hence, the time delay is not taken into account. The potential mutual interaction between the landing gear and the fuselage is then studied for this coupled model, with special interest in the effect of different modal masses; to this end numerical bifurcation analysis is used, specifically the continuation software AUTO.[15]

The analysis reveals that, when the forward velocity is varied, the straight rolling solution

loses its stabilty via Hopf-bifurcations; the system can experience stable periodic oscillations dominated by either lateral or torsional oscillations of the NLG. It is also shown that, in general, the lower the modal mass, the higher the amplitude of the emerging fuselage vibrations, hence, the more energy is fed into the fuselage from the NLG. On the other hand, a change in the modal mass not only changes the fuselage amplitudes, but also influences the regions of stability and, at certain velocities, the type of oscillation; i.e. a dominantly torsional oscillation can change to lateral- or even quasi-periodic oscillations. However, this effect is strongly influenced by the load as well. To show these results in detail, one- and two-parameter bifurcation diagrams are presented.

II. The Model

II.A. A low-order fuselage model

Due to the nature of the NLG-fuselage system, a coupled, constrained model is required, that incorporates separate models for both the NLG and the fuselage, and is completed by the tyre model. Both the NLG model of [12] – the configuration of which is used here –, and the tyre model are highly nonlinear. Owing to low fuselage amplitudes, a low order, linear model is used to represent the fuselage dynamics. Out of the many considerable modes of a fuselage, only those with lateral displacement component at the attachment point are considered in this study. That displacement can be the result of either a modal oscillation leading to deformation at the front of the fuselage or, alternatively, a rigid body mode corresponding to the torsional oscillation of the fuselage about its vertical body axis; see Figure 1.

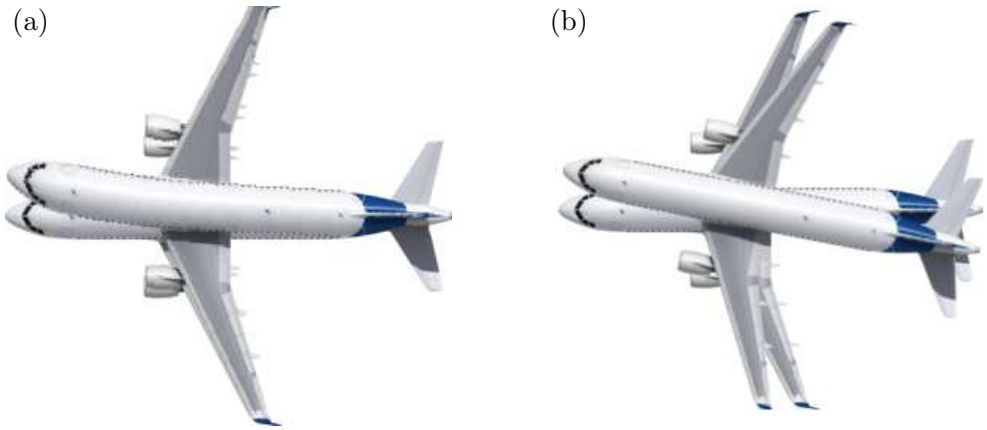

Figure 1: Illustrations of the considered fuselage dynamics. Panel (a) and (b) show modes with exagerrated lateral deformation of the fuselage, and rigid body oscillation about the vertical body axis, respectively.

In the first case we assume an elastic fuselage and allow modal dynamics, whereas in

the second case we assume that, while moving forward on the runway, the aircraft oscillates torsionally about its centre of mass as a rigid body. In either case, the amplitudes of oscillations are assumed to be small compared to the wheelbase of the aircraft. Therefore, the motion of the attachment point is taken as linear translation and, hence, its dynamics is modelled by a linear mass-spring-damper system (MSD). It is characterized by its natural frequency f_n, relative damping q and modal mass μ corresponding to the considered mode, and also by the lateral fuselage displacement y. Moreover, the mass is allowed to move up and down introducing a vertical displacement z; however, this motion is constrained to follow the vertical component of translation of the top of the landing gear system, which leaves y as the only fuselage degree-of-freedom; see Section II.C for details of the vertical constraint. Further, the proportion of the weight M of the aircraft, that is supported by the NLG, when the aircraft is on the ground, and the weight m of the NLG are considered by the corresponding gravitational forces.

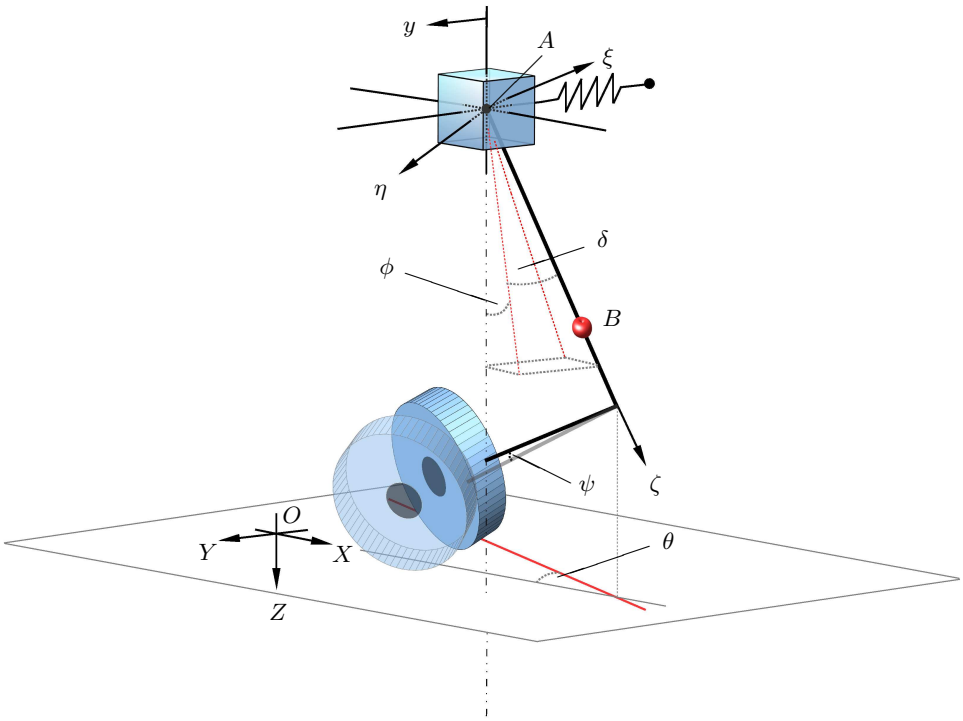

Figure 2: Schematic representation of a nose landing gear with a lateral mass-spring-damper system

II.B. The landing gear model

The coupled NLG-fuselage model is shown in a non-equlibrium state in Figure 2. The landing gear model consists of the wheel/tyre, the caster and the strut with a combined centre of

gravity at B, assumed to lie on the axis of the strut. The MSD is attached to the top of the strut at its centre of gravity A. The gravitational forces $\mathbf{G}_A$ and $\mathbf{G}_B$ correspond to the weights M and m acting at points A and B, respectively.

In order to describe the geometric and kinematic properties of the system, three frames of reference are used. One is a moving frame (referred to as the *body frame*), which is fixed to the landing gear with the origin at the attachment point A. Its axes are denoted ξ, η and ζ. Here, the axis ζ is in line with the strut at all times and points from point A to the centre of gravity B of the NLG. The axis ξ is parallel with the caster – defined as being at 90° to the strut – pointing out of the NLG, and η completes the right-handed coordinate system. The strut is inclined to the vertical at a fixed rake angle ϕ and allowed to rotate about the body axis ζ with the torsion angle ψ. Moreover, it may rotate in the lateral direction around the body axis ξ as described by the bending angle δ. Hence, ψ and δ are the two NLG degrees-of-freedom. Further, the strut is modelled as having torsional and lateral stiffnesses and dampings at the attachment point A. Another frame (referred to as the *global frame*) is fixed to the ground with origin O and axes X,Y and Z. Here, Z is the vertical axis pointing downwards, X points in the direction of aircraft motion and Y completes the right-handed coordinate system.When $\psi = \delta = y = 0$, that is, in the undisturbed condition, the X-axis is aligned with the central line of the tyre and A lies in the (X, Z)-plane. The third frame (referred to as the *tyre frame*) is a local frame used to describe the tyre deflection; see Figure 3. Its origin is at point C, which is determined as the intersection of three intersecting planes. They are the wheel plane, the ground and the plane, that is normal to the ground and includes the wheel centre point. The axes of the tyre frame are x and λ, where λ is the perpendicular deflection of the points of the contact line with respect to the wheel plane-ground intersection.

II.C. Kinematics of the coupled system

Rolling without sliding results in a kinematic constraint on the system. In order to derive this constraint the wheel-ground interface is to be considered. It is derived from the assumed condition of the tyre fully adhering to the ground at all times. This means that the absolute velocities of points along the contact line and, in particular, that of the leading contact point is zero. In order to derive that velocity in terms of the states, the kinematics of the entire system must be analysed.

The motion of the lumped mass is three dimensional translation. It is a combination of the steady-state forward motion along the X-axis at constant velocity V_x, the harmonic oscillation in the Y-direction and a constrained vertical motion in the Z-direction; the tyre is assumed to be rigid in radial direction and, hence, as the NLG and the tyre move, the attachment point A must move vertically to maintain ground contact. The motion of the

NLG is genuinely three dimensional. However, since the NLG is suspended by the lumped mass, and the motion relative to the attachment point A is a rotation about a fixed point, the absolute motion can be described by means of relative kinematics. First, the absolute kinematics of the lumped mass and the relative kinematics of the NLG – with respect to the lumped mass – are derived. Then the absolute kinematics of the NLG and, hence, that of the centre of the wheel, can be obtained. Further, by deriving the relative motion of the leading contact point with respect to the wheel plane-ground intersection, the absolute velocity of the leading point and, hence, the required constraint, can be given.

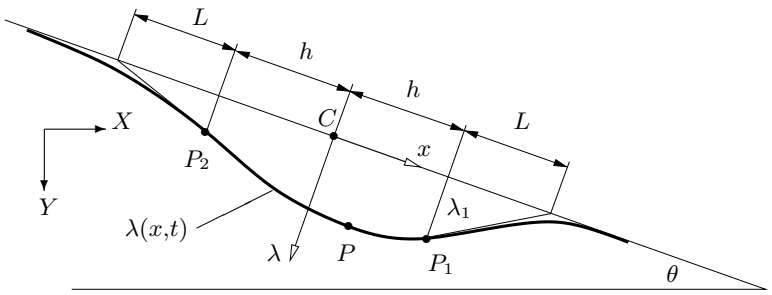

Figure 3: Tyre deformation according to the stretched string tyre model. The turning angle θ is between the direction of motion X and the intersection of the ground and the wheel plane

Since the natural frame for the MSD is the global frame, this frame is chosen for the derivations and, therefore, the NLG states must be transformed into the global frame from the moving frame. The instantaneous position of the NLG and, hence, of the centre of the wheel, with respect to the global frame can be described as the result of three sequential rotations: a rotation about the Y-axis due to the non-zero but time-independent rake angle ϕ, followed by a rotation of δ about the rotated X-axis and, finally, a rotation of ψ about the strut axis. The Euler-transformation that gives the transformation from the body frame to the global frame, considering this particular order of rotations (ϕ, δ, ψ), in matrix form is given by

$$\mathbf{T} = \begin{bmatrix} \cos\phi\cos\psi + \sin\phi\sin\delta\sin\psi & -\cos\phi\sin\psi + \sin\phi\sin\delta\cos\psi & \cos\delta\sin\phi \\ \cos\delta\sin\psi & \cos\delta\cos\psi & -\sin\delta \\ -\sin\phi\cos\psi + \cos\phi\sin\delta\sin\psi & \sin\phi\sin\psi + \cos\phi\sin\delta\cos\psi & \cos\delta\cos\phi \end{bmatrix}.$$

For the kinematic constraint to be derived, the position of a contact point P along the contact line, in the global frame, is to be derived first. It is given by

$$\mathbf{r}_{OP} = \mathbf{r}_{OA} + \mathbf{r}_{AC} + \mathbf{r}_{CP}. \tag{1}$$

That is, the position vector of P in the global frame is the superposition of the vectors pointing from the origin O to the attachment point A, from the attachment point A to the intersection point C, and from the intersection point C to the contact point P.

The position of the attachment point A is given by

$$\mathbf{r}_{OA} = \begin{bmatrix} V_x\, t \\ y \\ -L + z \end{bmatrix}, \tag{2}$$

where $L = l_{cw} + R$ is the distance of the attachment point A from the ground in the equilibrium position. Here, R is the wheel radius and l_{cw} is the distance from the wheel centre to the attachment point. The vector $\mathbf{r}_{AC}$ in the body frame is given by

$$\mathbf{r}^b_{AC} = \begin{bmatrix} -\left(e + R\sin\phi\right) \\ 0 \\ l_{cw} + R\cos\phi \end{bmatrix}, \tag{3}$$

where e is the caster length, and which, when transformed to the global frame, becomes

$$\mathbf{r}_{AC} = \mathbf{T}\,\mathbf{r}^b_{AC} = \begin{bmatrix} -\left(\cos\phi\cos\psi + \sin\phi\sin\delta\sin\psi\right)\left(e + R\sin\phi\right) + \cos\delta\sin\phi\left(l_{cw} + R\cos\phi\right) \\ -\cos\delta\sin\psi\left(e + R\sin\phi\right) - \sin\delta\left(l_{cw} + R\cos\phi\right) \\ \left(\sin\phi\cos\ \psi - \cos\phi\sin\delta\sin\psi\right)\left(e + R\sin\phi\right) + \cos\delta\cos\phi\left(l_{cw} + R\cos\phi\right) \end{bmatrix}. \tag{4}$$

In order to determine the vector $\mathbf{r}_{CP}$, the tyre model needs to be considered.

II.C.1. Tyre kinematics and global constraints

According to the exact stretched string model, the actual shape of the contact line is taken into account. Therefore, in the tyre frame, the deflection λ from the wheel plane-ground intersection of any contact point P between the leading point P_1 and the trailing point P_2 is given as a two-variable function $\lambda(x,t), x \in [-h,h]$ of space and time; see Figure 3. The vector $\mathbf{r}_{CP}$ in the global frame is, therefore, given by

$$\mathbf{r}_{CP} = \mathbf{r}_{CP}(x,t) = \begin{bmatrix} x\cos\theta - \lambda(x,t)\sin\theta \\ x\sin\theta + \lambda(x,t)\cos\theta \\ 0 \end{bmatrix} \tag{5}$$

for $x \in [-h,h]$, where the angle θ is the actual turning angle of the wheel on the ground. Due to the non-zero rake angle ϕ and the interacting lateral bending angle δ, it is different from the torsion angle ψ, and is given as $\theta = \psi\,\cos\delta\,\cos\phi$.

When superimposing the vectors (2),(4) and (5), the global position of P becomes

$$\mathbf{r}_{OP} = \begin{bmatrix} V_x t + r_{AC}^X + x\cos\theta - \lambda\,(x,t)\sin\theta \\ y + r_{AC}^Y + x\sin\theta + \lambda\,(x,t)\cos\theta \\ -L + z + r_{AC}^Z \end{bmatrix}, \tag{6}$$

where r_{AC}^X, r_{AC}^Y and r_{AC}^Z denote the respective coordinates of (4). When differentiated with respect to time, equation (6) leads to the velocity of P, which is given by

$$\mathbf{v}_P = \dot{\mathbf{r}}_{OP} = \begin{bmatrix} V_x + \dot{r}_{AC}^X + \dot{x}\cos\theta - x\,\dot{\theta}\sin\theta - \frac{d}{dt}\lambda\,(x,t)\sin\theta - \lambda\,(x,t)\,\dot{\theta}\cos\theta \\ \dot{y} + \dot{r}_{AC}^Y + \dot{x}\sin\theta + x\,\dot{\theta}\cos\theta + \frac{d}{dt}\lambda\,(x,t)\cos\theta - \lambda\,(x,t)\,\dot{\theta}\sin\theta \\ \dot{z} + \dot{r}_{AC}^Z \end{bmatrix}, \tag{7}$$

where

$$\begin{aligned}
\dot{r}_{AC}^X &= (\cos\phi\sin\psi - \sin\phi\sin\delta\cos\psi)\,(e + R\sin\phi)\,\dot{\psi} - (\sin\phi\cos\delta\sin\psi\,(e + R\sin\phi) \\
&\quad + \sin\delta\sin\phi\,(l_{cw} + R\cos\phi))\,\dot{\delta} \\
\dot{r}_{AC}^Y &= -\cos\delta\cos\psi\dot{\psi}\;(e + R\sin\phi) + (\sin\delta\sin\psi\,(e + R\sin\phi) - \cos\delta\,(l_{cw} + R\cos\phi))\,\dot{\delta} \\
\dot{r}_{AC}^Z &= -(\sin\phi\sin\psi + \cos\phi\sin\delta\cos\psi)\,(e + R\sin\phi)\,\dot{\psi} - (\cos\phi\cos\delta\sin\psi\,(e + R\sin\phi) \\
&\quad + \sin\delta\cos\phi\,(l_{cw} + R\cos\phi))\,\dot{\delta}
\end{aligned}$$

and $\frac{d}{dt}\lambda\,(x,t)$ is the total derivative of $\lambda\,(x,t)$ with respect to time, given by

$$\frac{d}{dt}\lambda\,(x,t) = \dot{\lambda}\,(x,t) + \lambda'\,(x,t)\,\dot{x}. \tag{8}$$

Here, $\dot{\lambda}\,(x,t)$ and $\lambda'\,(x,t)$ are the partial derivatives with respect to t and x, respectively.

The starting point of the derivation was the condition of full tyre adhesion, that is, $\mathbf{v}_P = \mathbf{0}$, which leads to the following scalar constraint equations:

$$V_x + \dot{r}^X_{AC} + \dot{x}\cos\theta - x\,\dot{\theta}\sin\theta - \Big(\dot{\lambda}\,(x,t) + \lambda'\,(x,t)\,\dot{x}\Big)\sin\theta - \lambda\,(x,t)\,\dot{\theta}\cos\theta = 0 \tag{9}$$

$$\dot{y} + \dot{r}^Y_{AC} + \dot{x}\sin\theta + x\,\dot{\theta}\cos\theta + \Big(\dot{\lambda}\,(x,t) + \lambda'\,(x,t)\,\dot{x}\Big)\cos\theta - \lambda\,(x,t)\,\dot{\theta}\sin\theta = 0 \tag{10}$$

$$\dot{z} + \dot{r}^Z_{AC} = 0 \tag{11}$$

Equation (11) is uncoupled from equations (9) and (10) and it reveals the constraint that governs the vertical displacement z of the fuselage. On the other hand, the coupled set of equations (9) and (10) – when solved for $\dot{\lambda}\,(x,t)$ – corresponds to the constraint of the lateral displacement of P on the contact line. The solution is a partial differential equation and is given by

$$\dot{\lambda}\,(x,t) = (V_x + \dot{r}^X_{AC})\sin\theta - (\dot{y} + \dot{r}^Y_{AC})\cos\theta - x\,\dot{\theta} + \lambda'\,(x,t)\,\Big(\lambda\,(x,t)\;\dot{\theta} - (V_x + \dot{r}^X_{AC})\cos\theta - (\dot{y} + \dot{r}^Y_{AC})\sin\theta\Big). \tag{12}$$

However, we are only interested in the lateral displacement of the leading point P_1, that is, when $x = h$. In that case, equation (12) can be simplified by the application of the boundary condition

$$\lambda'\,(x,t)\big|_{x=h} = -\frac{\lambda_1(t)}{L}. \tag{13}$$

Therefore, after substitutions, the final form of the constraint equation that describes the kinematics of the tyre becomes an ordinary differential equation, and is given by

$$\dot{\lambda}\,(x,t)\Big|_{x=h} = \dot{\lambda}_1 = (V_x + \dot{r}^X_{AC})\left(\sin\theta - \frac{\lambda_1}{L}\cos\theta\right) - (\dot{y} + \dot{r}^Y_{AC})\left(\cos\theta + \frac{\lambda_1}{L}\sin\theta\right) - \left(h - \frac{{\lambda_1}^2}{L}\right)\dot{\theta}, \tag{14}$$

where, for simplicity, λ_1 denotes $\lambda_1(t)$. With equations (11) and (14) both constraints are identified.

II.D. Equations of motion

During the derivation of the equations of motion, beside the real degrees-of-freedom y, δ and ψ, the vertical lumped mass displacement z is taken as a degree-of-freedom too – i.e. the constraint condition (11) is initially ignored. This approach is necessary in order to derive the reaction forces at the wheel–ground interface, and allows for a more concise derivation of the equations of motion. The constraint condition is then applied at the end of the derivation to eliminate z. The different parameters and their values can be found in Table 1.

For each degree-of-freedom the Lagrangian equation

$$\frac{\partial}{\partial t}\frac{\partial T}{\partial \dot{q}_i} - \frac{\partial T}{\partial q_i} + \frac{\partial V}{\partial q_i} + \frac{\partial D}{\partial \dot{q}_i} = Q_i \tag{15}$$

holds, where T is the kinetic energy, V is the potential energy, D is the dissipative energy, Q_i is the generalized force and q_i is the generalized coordinate.

The kinetic energy of the system is

$$T = \frac{1}{2}\,\mu\,(v_A^Y)^2 + \frac{1}{2}\,M\left((v_A^X)^2 + (v_A^Z)^2\right) + \frac{1}{2}\,m\,|\mathbf{v}_B|^2 + \frac{1}{2}\,\boldsymbol{\omega}_B{}^T\mathbf{J}_B\,\boldsymbol{\omega}_B, \tag{16}$$

where, v_A^X, v_A^Y and v_A^Z are the respective global coordinates of the absolute velocity $\mathbf{v}_A$ of A, $\mathbf{v}_B$ is the absolute velocity of B, $\boldsymbol{\omega}_B$ is the absolute angular velocity of the landing gear and $\mathbf{J}_B$ is the mass moment of inertia tensor of the NLG at B, in the global frame. Equation (16) is based on the modal mass μ being active only in the lateral direction, whereas the mass M is active in the forward and vertical directions. The gyroscopic effect of the wheel is not considered here, because the focus of our investigation is on the interacting motions in the structure due to geometry (for a detailed discussion on those effects on a landing gear – in the absence of fuselage motion – see [16]) . Therefore, the corresponding kinetic energy is zero, which is in line with previous work; see [12].

The vector $\mathbf{v}_A$ is the derivative of (2); it is given by

$$\dot{\mathbf{r}}_{OA} = \mathbf{v}_A = \begin{bmatrix} V_x \\ \dot{y} \\ \dot{z} \end{bmatrix}. \tag{17}$$

The absolute velocity of B is the superposition of the absolute velocity of A and the relative velocity of B with respect to A, that is,

$$\mathbf{v}_B = \mathbf{v}_A + \mathbf{v}_{AB}, \tag{18}$$

where

$$\mathbf{v}_{AB} = \boldsymbol{\omega}_{AB} \times \mathbf{r}_{AB}. \tag{19}$$

Here, $\mathbf{r}_{AB}$ is the relative position of B with respect to A; in the body frame it is given by

$$\mathbf{r}_{AB}^b = \begin{bmatrix} 0 \\ 0 \\ l_\zeta \end{bmatrix}, \tag{20}$$

where l_ζ is the distance from the attachment point A to the centre of gravity B. When transformed to the global frame, equation (20) becomes

$$\mathbf{r}_{AB} = \mathbf{T}\,\mathbf{r}^b_{AB} = \begin{bmatrix} l_\zeta \cos\delta \sin\phi \\ -l_\zeta \sin\delta \\ l_\zeta \cos\delta \cos\phi \end{bmatrix}. \tag{21}$$

The vector $\boldsymbol{\omega}_{AB}$ in (19) is the relative angular velocity of the NLG with respect to the lumped mass. Since there is a sequence of rotations taking place in sequentally rotated body frames, the individual rotation vectors do not form an orthogonal set, and so $\boldsymbol{\omega}_{AB}$ can only be expressed by superimposing the individual rotations transformed separately to one of the reference frames. Consequently, the relative angular velocity in the global frame is given by

$$\boldsymbol{\omega}_{AB} = \begin{bmatrix} \dot\delta \cos\phi + \dot\psi \cos\delta \sin\phi \\ -\dot\psi \sin\delta \\ -\dot\delta \sin\phi + \dot\psi \cos\delta \cos\phi \end{bmatrix}. \tag{22}$$

Therefore, after substitutions into (18), the absolute velocity of B becomes

$$\mathbf{v}_B = \begin{bmatrix} V_x - \dot\delta l_\zeta \sin\delta \sin\phi \\ \dot y - \dot\delta l_\zeta \cos\delta \\ \dot z - \dot\delta l_\zeta \sin\delta \cos\phi \end{bmatrix}. \tag{23}$$

The angular velocity of the MSD is zero; hence, the absolute angular velocity of the landing gear is

$$\boldsymbol{\omega}_B = \boldsymbol{\omega}_{AB}, \tag{24}$$

and so all terms in equation (16) are determined. The potential energy is

$$V = \frac{1}{2}\,k_\delta \delta^2 + \frac{1}{2}\,k_\psi \psi^2 + \frac{1}{2}\,k_y y^2, \tag{25}$$

where k_δ, k_ψ and k_y are the respective stiffnesses. The Rayleigh-function for the dissipated energy is given by

$$D = \frac{1}{2}\,c_\delta \dot\delta^2 + \frac{1}{2}\,c_\psi \dot\psi^2 + \frac{1}{2}\,c_y \dot y^2, \tag{26}$$

where c_δ, c_ψ and c_y are the respective dampings of the system. After obtaining the equations of motion, the parameters k_y and c_y are replaced by the natural frequency f_n and relative

damping q, respectively and, hence, their values are not given.

The generalized forces Q_i are calculated from the virtual power of the active forces and moments acting on the system and are given by

$$Q_i = \sum_{j=1}^{N} \mathbf{F}_j \cdot \frac{\partial \mathbf{v}_j}{\partial \dot{q}_i} \qquad i \in \{y, z, \delta, \psi\} \tag{27}$$

Here, N is the total number of active forces and moments and $\mathbf{F}_j$ and $\mathbf{v}_j$ are the force/moment and velocity vectors at the point of action, respectively, for each active force and moment. The active forces and moments are the gravitational forces $\mathbf{G}_A$ and $\mathbf{G}_B$, given by

$$\mathbf{G}_A = \begin{bmatrix} 0 \\ 0 \\ Mg \end{bmatrix}, \quad \mathbf{G}_B = \begin{bmatrix} 0 \\ 0 \\ mg \end{bmatrix}, \tag{28}$$

respectively, and the self aligning moment $\mathbf{M}_{K_\alpha}$ and lateral tyre force $\mathbf{F}_y$ due to the elasticity of the tyre, given by

$$\mathbf{M}_{K_\alpha} = \begin{bmatrix} 0 \\ 0 \\ -C_{K_\alpha} F_z \end{bmatrix}, \quad \mathbf{F}_y = \begin{bmatrix} -\Lambda F_z \sin\theta \\ \Lambda F_z \cos\theta \\ 0 \end{bmatrix}, \tag{29}$$

respectively. Here the coefficients C_{K_α} and Λ are given by

$$C_{K_\alpha} = \begin{cases} k_\alpha \frac{\alpha_m}{\pi} \sin\left(\alpha \frac{\pi}{\alpha_m}\right) & \text{if } |\alpha| \leq \alpha_m, \\ 0 & \text{if } |\alpha| > \alpha_m, \end{cases} \tag{30}$$

and

$$\Lambda = k_\lambda \arctan\left(7.0 \tan\alpha\right) \cos\left(0.95 \arctan\left(7.0 \tan\alpha\right)\right), \tag{31}$$

where k_λ, k_α and α_m are tyre parameters and α=arctan(λ/L) is the slip angle. The original functions of (30) and (31) are defined by Somieski[10] and are both piecewise continuous functions. Although the coefficient (30) is used here in the original form, the piecewise continuous function of (31) has been replaced by a fitted continuous function introduced by Thota et al. [12] As Equations (29) show, both $\mathbf{M}_{K_\alpha}$ and $\mathbf{F}_y$ are functions of the magnitude F_z of the vertical reaction force $\mathbf{F}_z$ at the wheel-ground interface, which is the reaction to the weight and inertia of the system. The vector $\mathbf{F}_z$ is given by

$$\mathbf{F}_z = \begin{bmatrix} 0 \\ 0 \\ -F_z \end{bmatrix}. \tag{32}$$

Since the vertical ground constraint (11) is not applied at this stage, $\mathbf{F}_z$ is considered as an independent external, active force – one which has virtual power. Once the missing constraint is established, $\mathbf{F}_z$ becomes the required reaction force. After substitution into (33), the generalized force is given by

$$Q_i = \mathbf{F}_z \cdot \frac{\partial \mathbf{v}_C}{\partial \dot{q}_i} + \mathbf{F}_y \cdot \frac{\partial \mathbf{v}_C}{\partial \dot{q}_i} + \mathbf{M}_{K_\alpha} \cdot \frac{\partial \boldsymbol{\omega}_B}{\partial \dot{q}_i} + \mathbf{G}_A \cdot \frac{\partial \mathbf{v}_A}{\partial \dot{q}_i} + \mathbf{G}_B \cdot \frac{\partial \mathbf{v}_B}{\partial \dot{q}_i}, \quad i \in \{y, z, \delta, \psi\}. \tag{33}$$

Here, $\mathbf{v}_C$ is the velocity of C in the global frame; it is given by

$$\mathbf{v}_C = \mathbf{v}_A + \mathbf{v}_{AC}, \tag{34}$$

where $\mathbf{v}_A$ is the absolute velocity of A – defined by equation (17) – and $\mathbf{v}_{AC}$ is the relative velocity of C with respect to A, given as the derivative of the relative position vector (4). After substitutions into (15), for $i = y,\delta,\psi,z$ respectively, the set of second-order equations of motion is

$$(\mu + m)\,\ddot{y} + \mu\left(2qf_n\dot{y} + {f_n}^2 y\right) - C_\delta\ddot{\delta} + S_\delta\dot{\delta}^2 - F_z\Lambda\cos\theta = 0, \tag{35}$$

$$J_1\ddot{\delta} + c_\delta\dot{\delta} + k_\delta\delta + J_2\ddot{\psi} + 2J_3\dot{\psi}\dot{\delta} + J_4\dot{\psi}^2 - C_\delta\ddot{y} + S_{\delta\phi}\,(g - \ddot{z}) + A_\delta F_z = 0, \tag{36}$$

$$J_5\ddot{\psi} + c_\psi\dot{\psi} + k_\psi\psi + J_2\ddot{\delta} - J_3\dot{\delta}^2 + A_\psi F_z = 0, \tag{37}$$

$$(M + m)\,\ddot{z} - S_\delta\ddot{\delta} - C_{\delta\phi}\dot{\delta}^2 - (M + m)\,g + F_z = 0, \tag{38}$$

where

$$S_\delta = ml_\zeta\sin\delta, \quad C_\delta = ml_\zeta\cos\delta, \quad S_{\delta\phi} = ml_\zeta\sin\delta\cos\phi, \quad C_{\delta\phi} = ml_\zeta\cos\delta\cos\phi,$$

and the coefficients A_δ and A_ψ are given by

$$\begin{aligned}
A_\delta &= (-\sin\delta\sin\psi\,(e+R\sin\phi)+\cos\delta\,(l_{cw}+R\cos\phi))\,\Lambda\cos\theta-\cos\phi\cos\delta\sin\psi\,(e+R\sin\phi)\\
&\quad-\sin\delta\cos\phi\,(l_{cw}+R\cos\phi)-(\sin\phi\cos\delta\sin\psi\,(e+R\sin\phi)+\sin\delta\sin\phi\,(l_{cw}+R\cos\phi))\,\Lambda\sin\theta\\
&\quad-C_{K_\alpha}\sin\phi,\\
A_\psi &= (\cos\phi\sin\psi-\sin\phi\sin\delta\cos\psi)\,(e+R\sin\phi)\,\Lambda\sin\theta+\cos\delta\cos\psi\,(e+R\sin\phi)\,\Lambda\cos\theta\\
&\quad-(\sin\phi\sin\psi+\cos\phi\sin\delta\cos\psi)\,(e+R\sin\phi)+C_{K_\alpha}\cos\delta\cos\phi.
\end{aligned}$$

The coefficients J_1-J_5 are transformed components of the mass moment of inertia tensor of the NLG at B ($\hat{\xi}$,$\hat{\eta}$ and $\hat{\zeta}$ are parallel to their body system counterparts ξ,η and ζ)

$$\begin{aligned}
J_1 &= \left(ml_\zeta^2+J_{\hat{\eta}\hat{\eta}}\right)+\left(J_{\hat{\xi}\hat{\xi}}-J_{\hat{\eta}\hat{\eta}}\right)\cos^2\psi-J_{\hat{\xi}\hat{\eta}}\sin(2\psi), \quad J_2=-J_{\hat{\eta}\hat{\zeta}}\sin\psi+J_{\hat{\xi}\hat{\zeta}}\cos\psi\\
J_3 &= \left(J_{\hat{\eta}\hat{\eta}}-J_{\hat{\xi}\hat{\xi}}\right)\cos\psi\sin\psi-J_{\hat{\xi}\hat{\eta}}\cos(2\psi), \quad J_4=-J_{\hat{\xi}\hat{\zeta}}\sin\psi-J_{\hat{\eta}\hat{\zeta}}\cos\psi, \quad J_5=J_{\hat{\zeta}\hat{\zeta}}.
\end{aligned}$$

From equation (38) the expression for F_z can be obtained. It is given by

$$F_z=(M+m)\,(g-\ddot{z})+S_\delta\ddot{\delta}+C_{\delta\phi}\dot{\delta}^2. \tag{39}$$

When substituting equation (39) into equations (35)-(37), F_z can be eliminated. Note, that due to not taking the vertical constraint (11) into account so far, the remaining equations still contain second-order terms of z. However, from the equation (11) $\ddot{z}$ can be obtained as

$$\ddot{z}=-\ddot{r}_{AC}^{z}=Z_1\ddot{\delta}+Z_2\dot{\delta}^2+Z_3\dot{\delta}\dot{\psi}+Z_4\dot{\psi}^2+Z_5\ddot{\psi}, \tag{40}$$

where Z_1-Z_5 are given by

$$\begin{aligned}
Z_1 &= \cos\phi\cos\delta\sin\psi\,(e+R\sin\phi)+\sin\delta\cos\phi\,(l_{cw}+R\cos\phi)\\
Z_2 &= -\cos\phi\sin\delta\sin\psi\,(e+R\sin\phi)+\cos\delta\cos\phi\,(l_{cw}+R\cos\phi)\\
Z_3 &= 2\cos\phi\cos\delta\cos\psi\,(e+R\sin\phi)\\
Z_4 &= (\sin\phi\cos\psi-\cos\phi\sin\delta\sin\psi)\,(e+R\sin\phi)\\
Z_5 &= (\sin\phi\sin\psi+\cos\phi\sin\delta\cos\psi)\,(e+R\sin\phi)
\end{aligned}$$

Therefore, z is eliminated from equations (35)-(37), resulting in the set of equations for y, δ and ψ given by

$$(\mu+m)\,\ddot{y}+\mu\left(2\,q\,f_n\dot{y}+{f_n}^2 y\right)-\left(C_\delta+\left(S_{\delta\phi}-(m+M)\,Z_1\right)\Lambda\,\cos\theta\right)\ddot{\delta}$$
$$+\left(S_\delta-\left(C_{\delta\phi}-(m+M)\,Z_2\right)\Lambda\,\cos\theta\right)\dot{\delta}^2+(m+M)\,Z_3\,\Lambda\,\cos\theta\dot{\delta}\dot{\psi}$$
$$+(m+M)\,Z_4\Lambda\,\cos\left(\theta\right)\dot{\psi}^2+(m+M)\,Z_5\Lambda\,\cos\left(\theta\right)\ddot{\psi}-(M+m)\,g\Lambda\,\cos\theta=0, \tag{41}$$

$$\left(A_\delta\left(S_{\delta\phi}-(m+M)\,Z_1\right)+J_1-S_{\delta\phi}Z_1\right)\ddot{\delta}+\left(A_\delta\left(C_{\delta\phi}-(m+M)\,Z_2\right)-S_{\delta\phi}Z_2\right)\dot{\delta}^2$$
$$+\left(2\,J_3-A_\delta\,(m+M)\,Z_3-S_{\delta\phi}Z_3\right)\dot{\delta}\dot{\psi}+\left(J_4-S_{\delta\phi}Z_4-A_\delta\,(m+M)\,Z_4\right)\dot{\psi}^2$$
$$+\left(J_2-A_\delta\,(m+M)\,Z_5-S_{\delta\phi}Z_5\right)\ddot{\psi}+\left(A_\delta\,(M+m)+S_{\delta\phi}\right)g+c_\delta\dot{\delta}+k_\delta\delta-C_\delta\ddot{y}=0, \tag{42}$$

$$\left(J_5-A_\psi\,(m+M)\,Z_5\right)\ddot{\psi}+\left(-J_3+A_\psi\left(C_{\delta\psi}-(m+M)\,Z_2\right)\right)\dot{\delta}^2-A_\psi\,(m+M)\,Z_4\dot{\psi}^2$$
$$+\left(A_\psi\left(S_{\delta\psi}-(m+M)\,Z_1\right)+J_2\right)\ddot{\delta}-A_\psi\,(m+M)\,Z_3\dot{\delta}\dot{\psi}+A_\psi\,(m+M)\,g+c_p\dot{\psi}+k_p\psi=0, \tag{43}$$

which, along with tyre equation (14), give a complete description of the NLG-fuselage system.

III. Bifurcation analysis

The main focus of the analysis is the interacting lateral fuselage and landing gear dynamics during take-off and landing. In terms of the model this means the study of the conditions for which the trivial straight-rolling solution $[y,\psi,\delta]^T=\mathbf{0}$ of equations (41)-(43) loses its stability; of interest are also the features of the emerging oscillatory behaviour. The aim is to identify parameter regions where the amplitude of the lateral displacement y and its impact on the rest of the system is significant. The equations of motion (41)-(43) with (14) are fully parametrized. They are studied here in terms of changes in the forward velocity V and two structural parameters: the modal mass μ of the MSD and the vertical mass load M. The parameters of the landing gear are fixed, as well as the natural frequency f_n and the relative damping q of the MSD; see Table 1.

In Figure 4 the result of time simulations of the system at $V=20$m/s, $\mu=3$t and $M=13$t is presented. After a transient, the system settles to a stable periodic solution, which is shown in terms of the ψ, δ, y and λ components in Figure 4a. This solution is dominated by oscillations of the torsional angle (with a maximum of $\psi\approx 8^\circ$) and, hence, is also is referred to as torsional shimmy oscillation. The motions of other degrees-of-freedom

Parameter	Name	Value
Fuselage data		
f_n	natural frequency	2 [Hz]
q	relative damping	0.02
Landing gear data		
l_ζ	distance from A to B	1.25[m]
m	mass of the landing gear	320 [kg]
$J_{\hat{\zeta}\hat{\zeta}}$	m.m. of inertia at B with respect to $\hat{\zeta}$-axis (axis through B)	100 [kg m^2]
$J_{\hat{\xi}\hat{\xi}}$	m.m. of inertia at B with respect to $\hat{\xi}$-axis (axis through B)	100 [kg m^2]
$J_{\hat{\eta}\hat{\eta}}$	m.m. of inertia at B with respect to $\hat{\eta}$-axis (axis through B)	100 [kg m^2]
$J_{\hat{\xi}\hat{\eta}}$	p. of inertia at B with respect to $(\hat{\xi}, \hat{\eta})$-axes (axes through B)	0 [kg m^2]
$J_{\hat{\xi}\hat{\zeta}}$	p. of inertia at B with respect to $(\hat{\xi}, \hat{\zeta})$-axes (axes through B)	0 [kg m^2]
$J_{\hat{\eta}\hat{\zeta}}$	p. of inertia at B with respect to $(\hat{\eta}, \hat{\zeta})$-axes (axes through B)	0 [kg m^2]
k_δ	lateral stiffnes of strut	6.1E6 [Nm rad^{-1}]
c_δ	lateral damping of strut	300 [Nms rad^{-1}]
k_ψ	torsional stiffnes of strut	3.8E5 [Nm rad^{-1}]
c_ψ	torsional damping of strut	300 [Nms rad^{-1}]
l_{cw}	distance from point A to the end of the strut	2.138 [m]
ϕ	rake angle	9 [°]
Tyre and wheel data		
R	wheel radius	0.362 [m]
L	relaxation length	0.3 [m]
e	caster length	0.12 [m]
k_λ	restoring coefficient of the tyre	0.002 [rad^{-1}]
h	half contact patch length	0.1 [m]
k_α	self-aligning coefficient of the tyre	1.0 [m rad^{-1}]
α_m	self-aligning moment limit	10[°]
Other		
g	gravitational acceleration	9.81 [m s^{-2}]

Table 1: System parameters

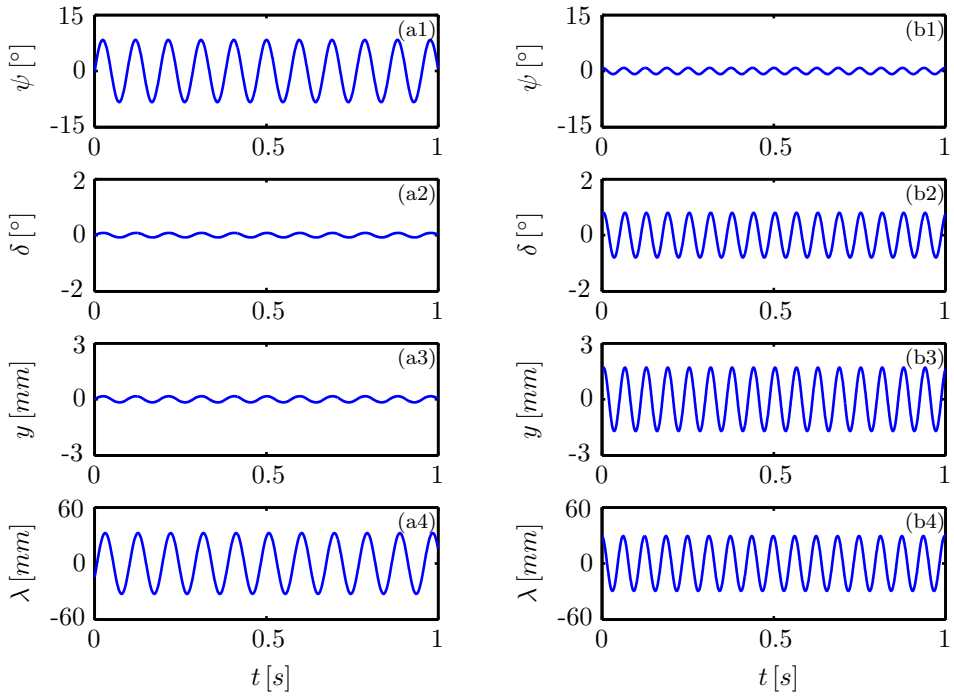

Figure 4: Coexisting torsional (column a) and lateral (column b) oscillations at $V = 20$m/s, $\mu = 3$t and $M = 13$t, shown as time series of the variables ψ, δ, y and λ.

remain damped, but the dominating oscillation is accompanied by oscillations of both the lateral angle and the lateral fuselage displacement, as well as of the lateral tyre displacement, all at the same frequency of $f \approx 10.5$Hz. This solution, however, is not unique due to the nonlinearities in the system. Perturbation can move the system to another stable periodic solution for which the lateral angle is dominant, while the motions of other degrees-of-freedom follow passively, at the frequency of oscillation of $f \approx 16.0$Hz; see Figure 4b. This solution is refered to as lateral shimmy oscillation. Figure 5 shows a time series of a stable trajectory for $V = 50$m/s. Here, the solution contains multiple frequencies, and the dominant one is different for the different states; the torsional angle ψ oscillates at close to the torsional frequency of $f \approx 10.8$Hz, whereas the lateral states δ and y oscillate at close to the lateral frequency of $f \approx 16.2$Hz. The tyre displacement λ, however, experiences coupled oscillation with two dominant frequencies.

III.A. One-parameter bifurcation analysis

The simulation results show that, for a given set of parameters, different behaviours of the system can be observed. However, since the behaviour depends on the initial conditions as well it is difficult to investigate all possible types of behaviour by simulation only. Therefore, the system is analysed further by means of numerical bifurcation analysis, specifically with

the continuation software AUTO.[15] To this end, in the simplest case, all but one parameter is fixed. The chosen parameter is called the continuation parameter. By continuously varying the continuation parameter the qualitative changes of the solutions can be studied (for details of bifurcation theory see for example [17]). Moreover, the difference between models with and without the additional lateral fuselage mode, can be revealed as well.

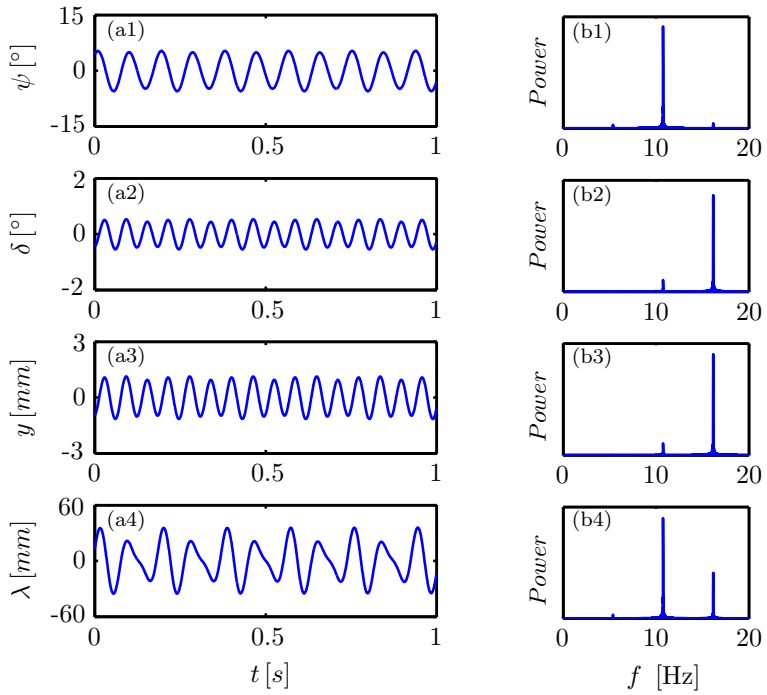

Figure 5: Multiple frequency oscillations at $V = 50$m/s, $\mu = 3$t and $M = 13$t, shown as time series of the variables ψ, δ, y and λ in panels (a1)-(a4) with associated frequency spectra in panels (b1)-(b4).

During take-off, the forward velocity V is one of the changing parameters. Since the onset of shimmy oscillations are observed at certain velocities, it is a natural choice to choose V as the continuation parameter.

Figure 6 shows a set of one-parameter bifurcation diagrams for $\mu = 3$t and $M = 13$t and for V as the continuation parameter. Each panel shows steady state solutions of the system for a state, plotted as a function of V. The solution measure is the maximum vibration amplitude. The different branches correspond to different types of solutions. These can either be equilibria with zero amplitude, referring to the straight rolling motion of the system, or periodic vibrations (referred as to periodic orbits) with single or multiple-frequency components. The diagrams in Figure 6 also indicate the stability of the solution; solid lines correspond to stable solutions, whereas dashed lines to unstable ones. A stable solution in this sense not only refers to the stable equilibrium (no oscillations), but also to

stable periodic orbits (constant maximum amplitude). Since Figure 6 shows what dynamics the system experiences at a continuous range of velocities, it gives a more global view of the system dynamics for a certain take-off scenario for a chosen fixed mass load M. At low velocities only stable equilibria exists, which means that the system is in stable straight forward rolling. At $V \approx 4.5$m/s this solution becomes unstable at a supercritical Hopf bifurcation H_t, and it regains stability at another Hopf-bifurcation H_l at $V \approx 180.0$m/s. From the Hopf-bifurcation point H_t a branch of periodic orbits, corresponding to torsional shimmy oscillations, emerges. This periodic branch is initially stable and the amplitudes gradually become larger as velocity increases. The dominance of the torsional motion at these low velocities can be captured by comparing the amplitudes of the states on the respective branches at the same velocity. A relatively small increment in V is enough for this periodic solution to lose its stabilty at a torus bifurcation T_t at $V \approx 5.4$m/s. It regains stability at another torus bifurcation T_t at $V \approx 14.6$m/s, and then it becomes unstable again at a third torus bifurcation T_t at $V \approx 41.2$m/s before the branch bifurcates with the unstable equilibrium at a Hopf bifurcation at $V \approx 75.6$m/s. The second branch of periodic solutions emerges from the unstable equilibrium branch at the Hopf bifurcation H_l at $V \approx 6.5$m/s. It is initially unstable but becomes stable when the torus bifurcation T_l at $V \approx 12.9$m/s is passed. The solutions along this branch are lateral shimmy oscillations. This branch also becomes unstable at a second torus bifurcation T_l at $V \approx 20.9$m/s, but regains stabilty at the torus bifurcation T_l at $V \approx 120.1$m/s. It remains stable until it joins the equlibrium branch at the previously mentioned Hopf-bifurcation H_l at $V \approx 180.0$m/s. There are also two branches of multiple-frequency periodic solutions (thin solid lines) which connect the two single frequency periodic branches. One emerges from the torisonal branch at the torus bifurcation T_t at $V \approx 5.4$m/s and joins the lateral branch at the torus bifurcation T_l at $V \approx 12.9$m/s. The other connects the two branches between the torus bifurcations T_t at $V \approx 41.2$m/s and T_l at $V \approx 120.1$m/s. These branches are calculated by a series of time simulations, since they can not readily be computed by continuation with AUTO. After identifying a point on the branch by running the simulation for long enough to get through the transient, the maximum amplitude of the resulting multiple-frequency oscillation is obtained. The next point is then calculated at a different V (sufficiently close to the previous value) by using the amplitudes of the previous solution as initial conditions for the new simulation. The final curves are interpolated splines, fitted to the obtained sequence of points. The main drawback of this method is that only stable branches can be calculated.

In Figure 6 one can follow the dynamics of the system when velocity increases. At low velocities the system is on the stable equlibrium branch, and so it experiences straight forward rolling. After losing stability at the first Hopf bifurcation H_t, torsional shimmy oscillation occur. As velocity increases, the amplitude of the oscillations become larger. However, this

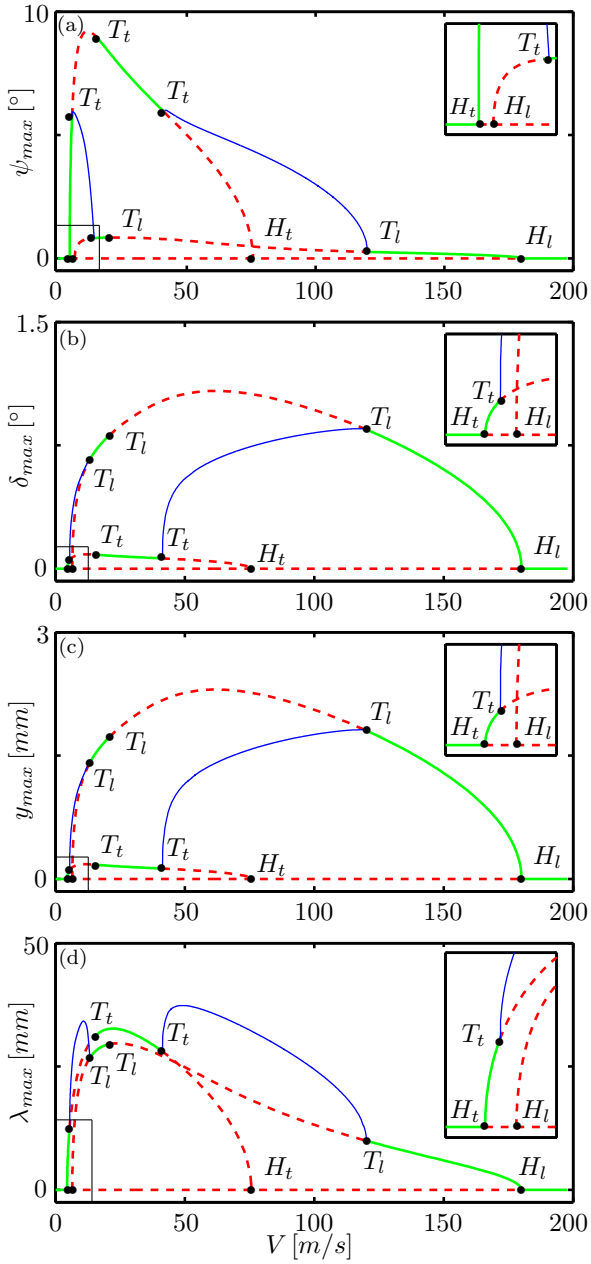

Figure 6: One-parameter bifurcation diagrams for $\mu = 3$t and $M = 13$t. Panels (a)-(d) show the maximum amplitude of the solution for δ, ψ, y and λ, respectively, plotted as a function of V. Solid and dashed lines represent stable and unstable solutions, respectively.

periodic oscillation too loses stability at the first torus bifurcation T_t, beyond which the system is attracted to the first multiple-frequency branch that connects the torsional and lateral branches. Since between the torus bifurcation points T_t and T_l this branch is the only stable one, the system follows that branch when velocity increases. Close to the torus bifurcation point T_t the torsional frequency component is significant; however, the further the velocity moves from T_t the more dominant the lateral component becomes. The dominance of the frequencies and, hence, the observed type of oscillation completely exchanges as the branch approaches the periodic branch of lateral solutions. This exchange can be seen in the amplitudes as well. Initially the system experiences torisonal shimmy with a torsional amplitude of $\psi \approx 5^\circ$ and negligible amplitudes of the lateral angle δ and lateral fuselage displacement y amplitudes. However, when moving along the multiple-frequency branch, the torsional amplitude becomes smaller, whereas the lateral amplitudes become larger. After passing the torus bifurcation point T_l, the system experiences single frequency lateral shimmy oscillation. However, since the torsional branch regains stability at $V = 14.6$m/s and the torsional branch loses it only at $V = 20.9$m/s, in between, two stable solutions exist. This means, that the right perturbation can move the system from one solution to the other. Indeed, Figure 4 shows two such coexisting solutions in this region. The end of this bistable region is reached with the second torus bifurcation T_l of the lateral branch, where the lateral solution loses stabilty. Passing this point the only remaining stable solutions are torsional shimmy opscillations and so the system necesserly jumps to them. When that solution too loses stabilty the system is attracted to another multiple-frequency branch, which – being the only stable branch – the system follows as velocity increases further, until the branch joins the single frequency lateral periodic branch. The solution shown in Figure 5 is from this region. From that velocity on the system experiences lateral shimmy up to the velocity where the branch bifurcates to the stable equilbrium branch at the Hopf bifurcation H_l. The value of V here, is well outside the range of realistic take-off or landing speeds; nevertheless, continuing the branches up to these high velocities makes the bifurcation diagrams complete and, hence, helps to understand the dynamics in the realistic range.

The same analysis can be performed for a different value of mass load M, while the modal mass is kept $\mu = 3$t. The results can then be compared, and the effect of the variation in M can be studied. Figure 7 shows the results for $M = 8$t. In this case as well, at low velocities, the only solution is the stable equilibrium. However, the first Hopf bifurcation occurs at a slightly higher velocity of $V \approx 7.5$m/s than in the previous case for $M = 13$t. The emerging periodic solutions are stable torsional shimmy oscillations with gradually larger amplitudes, although the amplitudes, in general, are smaller for this $M = 8$t case. However, this solution remains stable for a much greater range of velocities, and so the amplitude peaks at $V \approx 14.2$m/s and starts decreasing afterwards, as can best be seen

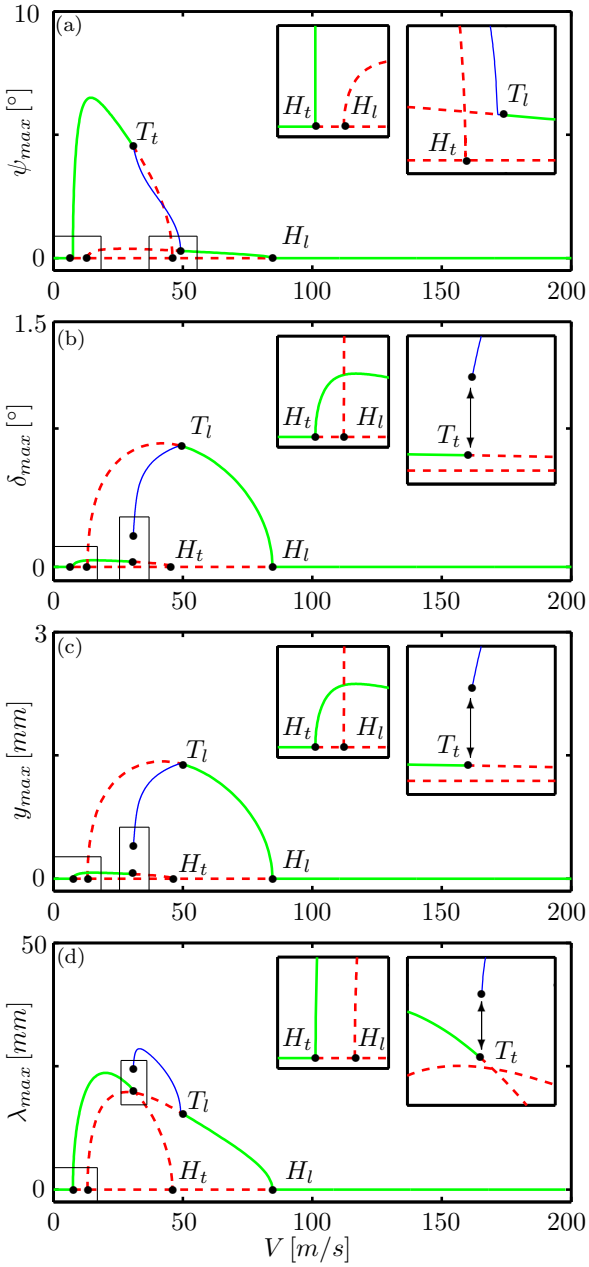

Figure 7: One-parameter bifurcation diagrams for $\mu = 3$t and $M = 8$t. Panels (a)-(d) show the maximum amplitude of the solution for δ, ψ, y and λ, respectively, plotted as a function of V. Solid and dashed lines represent stable and unstable solutons. Arrows denote very steep unstable multiple-frequency branches.

in Figure 7a. The torsional shimmy oscillation only loses its stability at $V \approx 30.6$m/s at the torus bifurcation T_t, and at $V \approx 45.9$m/s the unstable periodic branch bifurcates with the unstable equilibrium at the Hopf bifurcation H_t. The second branch of periodic solutions emerges again, from the unstable equilirium branch at the Hopf bifurcation H_l at $V \approx 13.1$m/s. This branch is initially unstable, becomes stable when the torus bifurcation T_l at $V \approx 49.1$m/s is passed and remains stable until joining the branch of equlibria at the Hopf bifurcation H_l at $V \approx 84.6$m/s. Due to the nature of stable and unstable branches, only one connecting multiple-frequency branch exists. However, the torus bifurcation T_t here is subcritical, meaning that the branch is initially unstable; it becomes stable very quickly at a velocity only marginally higher than that of the torus bifurcation T_t. The stable branch then joins the lateral branch at the torus bifurcation T_l. These multiple-frequency branches are again obtained by simulation. As discussed earlier, only the stable part of the branches are calculated in this way. Therefore, the unstable branch is represented by double-headed arrows, meaning that only the endpoints of the unstable branch is known, the actual curve in between is not. Notice, that this unstable part of the multiple-frequency branch appears to be very steep.

As Figure 7 shows, variation in the mass load M results in a qualitative change of the bifurcation diagram. For $M = 8$t, the torsional solution is dominant for a wider range of velocities, which means that, with increasing velocity, the system experiences torisonal shimmy oscillations with increasing amplitudes. Then the amplitude reaches a maximum and starts decreasing. Passing the torus bifurcation T_t the only stable branch of solutions is the multiple-frequency branch. Therefore, the system jumps to that branch and, hence, experiences multiple-frequency oscillations. The dominant oscillation gradually changes from torsional to lateral until it reaches the velocity of the torus bifurcation T_l, passing of which means that the system again experiences single frequency lateral oscillations. At the Hopf bifurcation H_l, the system returns to the straight forward rolling.

The two cases presented are different not only in terms of the type of single–multiple-frequency transition, but also in terms of the amplitudes and the range of velocities where the equilibrium (no shimmy) solution is stable. For the case of $M = 8$t the observed ampitudes are smaller in general, which also means that the considered fuselage mode is not excited as much as for $M = 13$t. On the other hand, the region of stable equilibrium solution is larger, indicating that the mass load has a destabilizing effect on the system; this is in agreement with previous work where the fuselage dynamics are not included; see [12].

III.B. Stability diagrams in the (V, M)-plane

In order to study more thoroughly how the mass load M effects the system, two-parameter continuation is performed in the continuation parameters V and M. This means that both

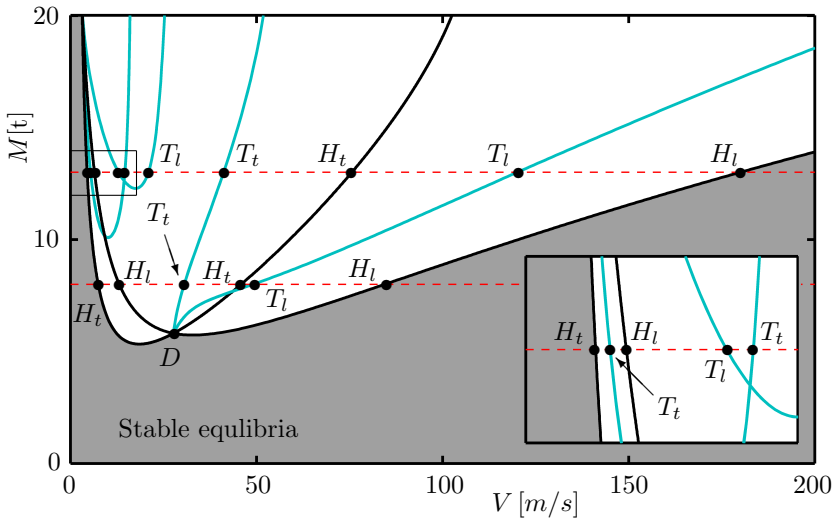

Figure 8: Two-parameter bifurcation diagram in the (V, M)-plane for $\mu = 3\text{t}$. Shown are (black) curves of Hopf bifurcation and (grey) curves of torus bifurcation; in the shaded region the straight-rolling solution is stable. The two dashed horizontal lines correspond to Figure 6 and Figure 7 for $M = 13\text{t}$ and $M = 8\text{t}$, respectively. The inset is an enlargement around $(V, M) = (9, 13)$.

V and M are now continuously changed, for a fixed value of parameter μ. The bifurcation diagram for $\mu = 3\text{t}$ and for a realistic range of mass load M is shown in Figure 8. Horizontal slices of the diagram correspond to one-parameter continuations for fixed mass M, and the red dashed lines correspond to the cases $M = 13\text{t}$ and $M = 8\text{t}$ in Figures 6 and 7. The two-parameter bifurcation diagram does not show the amplitudes of states, but labels the bifurcation points of Figure 6 and Figure 7 along the respective horizontal line. When continuously changing the value of mass load M, these bifurcation points generate bifurcation curves: Hopf bifurcation curves, H_t and H_l, and torus bifurcation curves, T_t and T_l, respectively. Further, the two Hopf bifurcation curves intersect at the double Hopf bifurcation point D; two of the four torus bifurcation curves emerge from this point. As Figure 6 and Figure 7 show, the stability of the equilibrium solution and, hence, the onset of shimmy oscillations is determined by the Hopf-bifurcations. Therefore, the Hopf bifurcation curves in Figure 8 define stability boundaries for the system. The shaded region represents all pairs of V and M, at which the equilibrium solution – corresponding to the straight-rolling motion – is stable.

The analysis so far has been performed at the fixed modal mass $\mu = 3\text{t}$. However, in order to study the effects of the introduced fuselage dynamics and its different characterics on the system, variation of the fuselage modal mass μ also needs to be considered. Figure 9 shows a set of two-parameter bifurcation diagrams in the (V, M)-plane for different values of μ. They are similar to the one in Figure 8, but have an extended M-axis. Extending

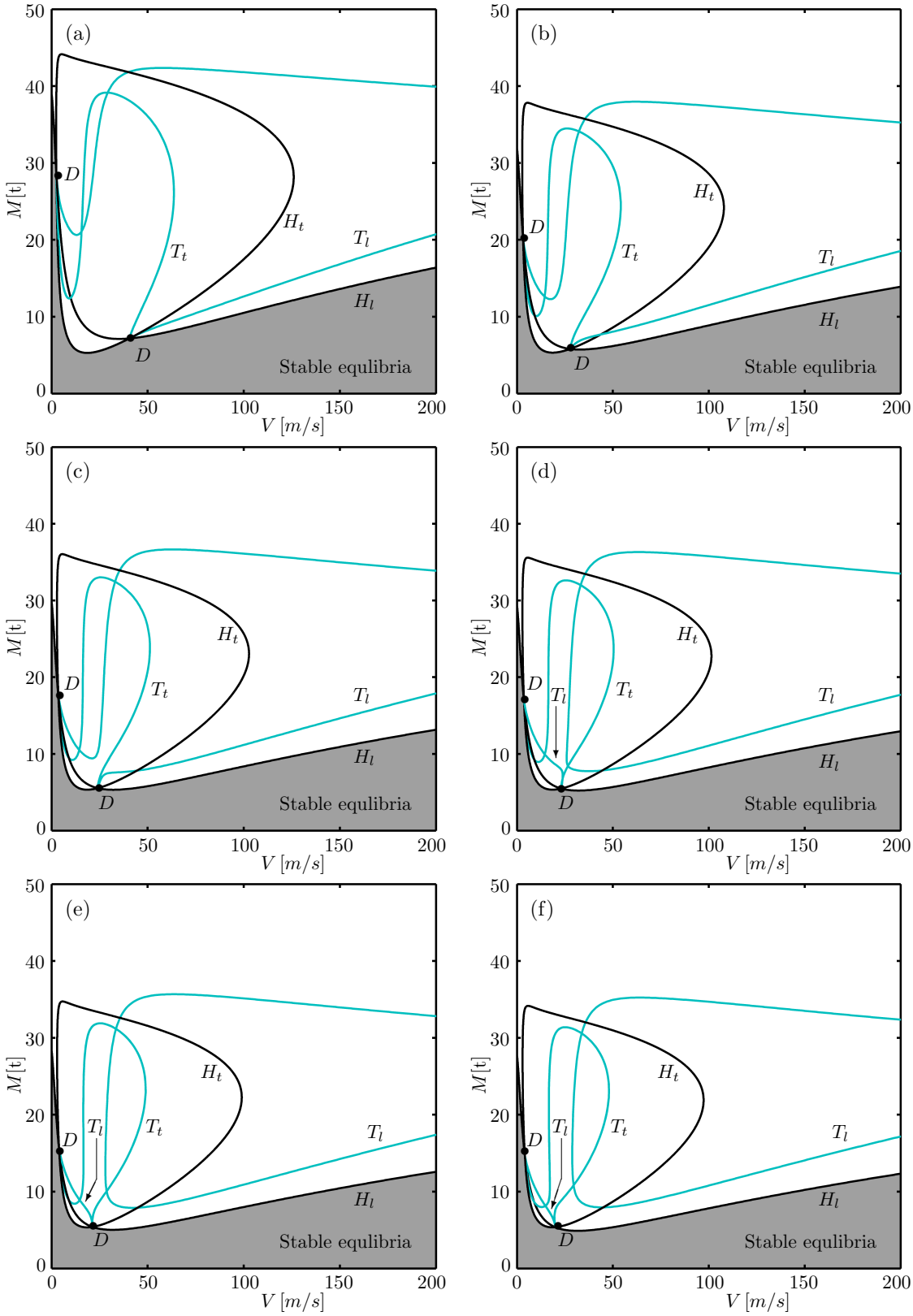

Figure 9: Two-parameter bifurcation diagrams in the (V, M)-plane for $\mu = 1\text{t}$ (a), $\mu = 3\text{t}$ (b), $\mu = 6\text{t}$ (c), $\mu = 8\text{t}$ (d), $\mu = 20\text{t}$ (e) and $\mu = 15000\text{t}$ (to approximate an infinitely large modal mass) (f). Shown are (black) curves of Hopf bifurcation and (light) curves of torus bifurcation; in the shaded region the straight-rolling solution is stable.

the axes beyond the realistic range gives a more global view on the arrangement of the curves and, therefore, helps to interpret the bifurcation diagram in the realistic range as well. Figure 9b corresponds to the case of $\mu = 3t$, from Figure 8 but over a larger range of M. Figure 9b shows that the Hopf bifurcation curve H_t in Figure 8 is actually an isola, and the Hopf bifurcation curve H_l intersects it at two double Hopf bifurcation points D. Over this extended range it can also be seen that two of the four torus curves in Figure 8 are connected, forming the torus bifurcation curve T_t. Moreover, this curve T_t connects the double Hopf bifurcation points. Further, each of the other two torus bifurcation curves T_l emerges from one of the double Hopf bifurcation points D. The sequence presented in Figure 9 shows how the relative positions of the curves and, hence, the region of stable equlibria evolves when the value of modal mass μ is changed from the rather small value of $\mu = 1$t to $\mu = 15000$t; the latter condition is an approximation of the case of μ tending to infinity, representing a laterally inactive fuslage. It can be seen that, as the modal mass μ increases, the isola becomes smaller. However, from its local minimum, $M \approx 5.3$t, to $M \approx 11$t the loci of the Hopf bifurcations do not change significantly. Above this load, the locus of the second Hopf bifurcation point, and so the maximum in V of the curve H_t moves to measurably lower velocity values. On the other hand, the curve H_l too moves towards the direction of smaller M values as μ becomes larger, which implies that the double Hopf bifurcation points D move towards smaller M and V values. The change of the torus bifurcation curves is more obvious. As μ increases the endpoints of the curves move closer to each other – due to the move of the secondary Hopf bifurcation points. Moreover, the loop of the curve T_t becomes narrower and the upper and lower T_l curves move closer to each other. At $\mu \approx 7.6$t the two separate T_l curves connect and split again right after, now in a different way; see Figure 9c and Figure 9d. They become a left and a right curve which move further apart as μ increases from $\mu = 8$t to $\mu = 20$t; see Figure 9d and Figure 9e. This topological change in the (V, M)-plane is due to a saddle transition of the T_l surface in the (V, M, μ)-space; see, for example [18, 19] for other examples of this transition. In Figure 9f the $\mu = 15000$t case is shown. The topology of the two-parameter bifurcation diagram is the same as that of the $\mu = 20$t case, although the loop of the torus bifurcation curve T_t is narrower and the two T_l bifurcation curves are further apart. This suggests that fuselage modes even with relatively large modal mass μ behave differently than the system with an inactive modal mass. In this regard, it is worth noting that the inactive modal mass case is effectively what is considered by Thota et al. in [12], where the fuselage motions are not taken into account. Qualtitatively the two models show good agreement. Both the isolated H_t bifurcation curve and the H_l bifurcation curve is present in both models; however, the size of the isola and the location of the bifurcation curve H_l with respect to the isola are somewhat different. This is due to the fact that in the model considered here, the vertical loads and reactions now affect both

the lateral and torsional motions instead of the torsional motion only. This is a consequence of the genuinely three-dimensional rotation of the NLG.

III.C. Stability diagrams in the (V, μ)-plane

As discussed in Section III.B, not only do the bifurcation diagrams in the (V, M)-plane show how changes in the modal mass μ affect the stability of the system, but the case approximating the inactive mass makes the connection with previous work[12] as well. Figure 9 also reveals that, due to the changing topology of the torus bifurcation curves T_t and T_l, the number of changes in the stability of the periodic solutions, and the velocities at which those happen, is affected by the variation of μ. However, the selected distinct values of μ do not appear to significantly affect the region of stable equlibria. In order to obtain a more general understanding of the dynamics related to the introduced fuselage dynamics, and to identify modal mass μ values, where the effect on the stable equilibria is significant, a second two-parameter analysis is performed, this time in V and μ for fixed values of M. A sequence of bifurcation diagrams in the (V, μ)-plane is shown in Figure 10, where the panels correspond to different fixed M values between $M = 7\text{t}$ and $M = 15\text{t}$. Here, all panels are composed of the same curves as those of Figure 9, although they are shown from a different perspective. The connection between Figure 10 and Figure 9 is made by the horizontal slices of different panels; i.e. the slice taken at $\mu = 3\text{t}$ in Figure 10a represents dynamics for the same parameters as that taken at $M = 7\text{t}$ in Figure 9b.

Figure 10a shows the bifurcation diagram for $M = 7\text{t}$. The isolated Hopf bifurcation curve H_t of Figure 9 now manifests itself as two separate curves H_t, while the Hopf bifurcation curve H_l is connected in the (V, μ)-plane as well. Again, the curves H_t and H_l intersect at the double Hopf bifurcation point D and a pair of torus bifurcation curves, T_t and T_l emerge from the these points. Due to the fact that there are now two curves H_t, the region of stable equilibrium solutions now consists of two components. The sequence of panels in Figure 10 shows how the arrangement changes due to the variation of the load M. As M increases, the region of stable equlibria shrinks. This is due to the descending curve H_l, but also to the fact that the curves H_t move further apart; this corresponds to the widening of the isola in Figure 9. The joint relocation of the curves also results in different locations of the double Hopf bifurcation point D and the appearing of another intersection point D in the region of interest when $M = 15\text{t}$; see Figure 10f. Further, the shape of the two torus bifurcation curves T_t and T_l changes significantly. The monotone curves in Figure 10a start to have local minima and maxima for larger values of M; see Figure 10b and Figure 10c. As M increases, the local minima and maxima move towards smaller and larger values of μ, respectively. Moreover, the maxima of the curves gradually move out of the region of interest; see Figure 10c and Figure 10d. The position of the minima are of importance in

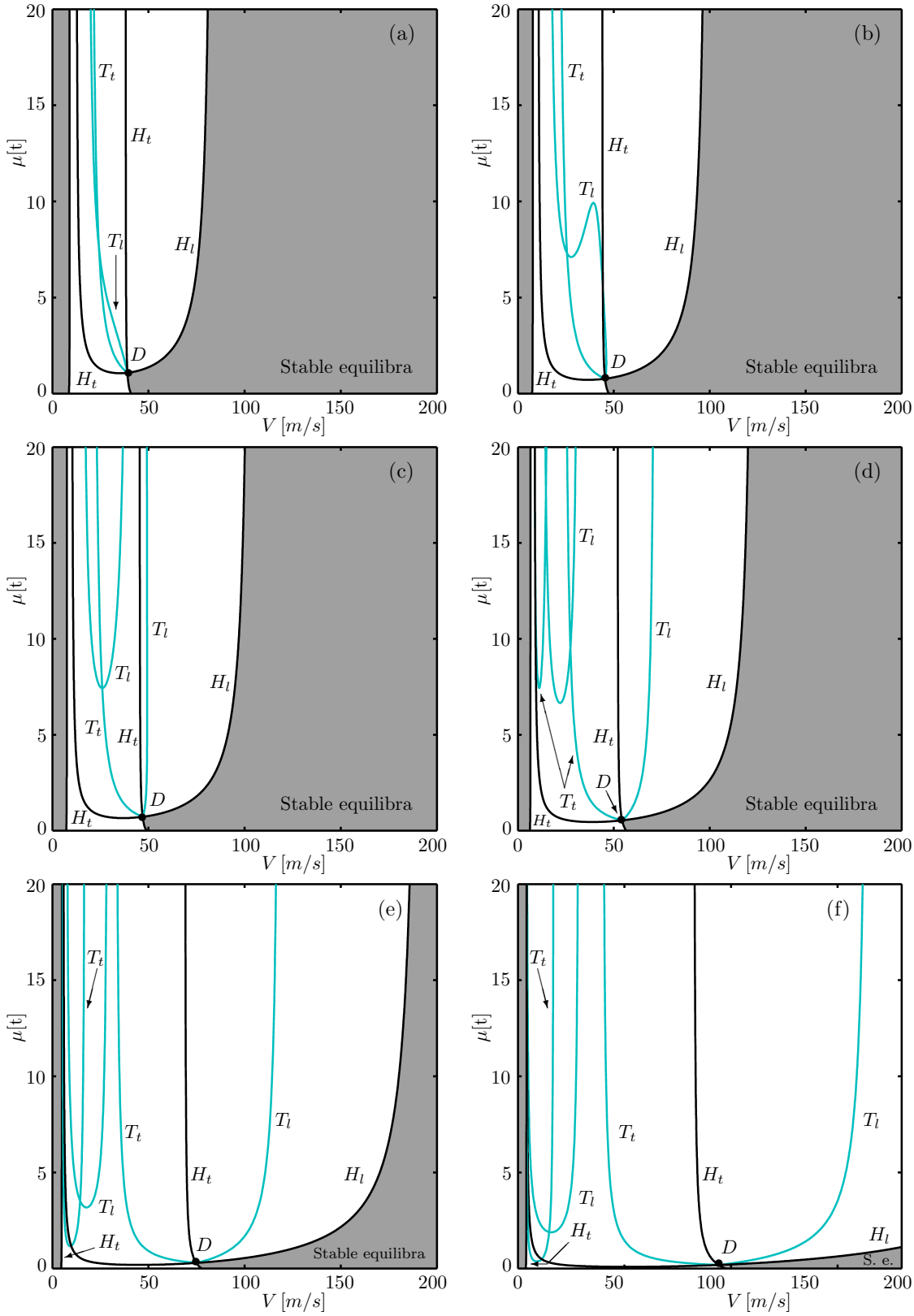

Figure 10: Two-parameter bifurcation diagrams in the (V, μ)-plane for $M = 7$t (a), $M = 7.8$t (b), $M = 8$t (c), $M = 9$t (d), $M = 12$t (e) and $M = 15$t (f). Shown are (black) curves of Hopf bifurcation and (light) curves of torus bifurcation; in the shaded regions the straight-rolling solution is stable.

terms of the dynamics of the system, because they define critical values of modal mass, below which stable branches of periodic solutions appear or disappear.

To illustrate this, Figure 11 presents for comparison a one-parameter bifurcation diagram for $M = 8$t and $\mu = 15000$t, that is, for the case of an inactive modal mass μ. In this case the MSD is not oscillating and, hence, the displacement y is always zero; see Figure 11c. Due to the fact that the modal mass is still present, albeit very large, there are oscillations in y (although their amplitudes are very tiny) and, therefore, the corresponding bifurcation points are still shown in Figure 11c. The stable straight rolling solution loses stability at a Hopf-bifurcation H_t at $V \approx 7.5$m/s and becomes stable again at a second Hopf-bifurcation H_t at $V \approx 103.4$m/s. The emerging torsional branch is initially stable, but loses stability at the torus bifurcation T_t at $V \approx 20.6$m/s; it remains unstable until it connects to the branch of unstable equlibria at the Hopf bifurcation H_t at $V \approx 45.3$m/s. The branch of lateral solutions, which emerges from the Hopf bifurcation H_l at $V \approx 10.0$m/s as initially unstable, becomes stable at the torus bifurcation T_l at $V \approx 15.2$m/s, but loses stabilty at the second torus bifurcation T_l at $V \approx 40.3$m/s. However, it regains stabilty at the third torus bifurcation T_l at $V \approx 48.9$m/s after a short gap of instability. The branch then remains stable until it bifurcates with the branch of stable equilibria at the second Hopf-bifurcation H_l. In this case as well, there is a region where the only stable solution is a muliple frequency solution. It is between the second and third torus bifurcation points T_l of the lateral branch, and so this multiple-frequency branch connects stable parts of the same periodic branch (unlike in case $\mu = 3$t, where the multiple-frequency branch connects stable parts of different braches). The torus bifurcations T_l are both subcritical, and so the stable part of the multiple-frequency branch is not connected directly to them. As for $\mu = 3$t, the unstable parts of the branch are represented by arrows. There is a region of bistability between $V \approx 15.2$m/s and $V \approx 20.6$m/s, where two stable periodic solutions coexist.

Let us reconsider now Figure 7 in comparison with Figure 11. Since both bifurcation diagrams belong to the same fixed mass load of $M = 8$t, the only difference in parameters between the two cases is the value of the modal mass μ. Therefore, the changes that an active modal mass may cause in the behaviour of the NLG-fuselage system compered to the inactive case, can be studied. One obvious difference between Figure 7 and Figure 11 is the activated oscillations of the MSD and, hence, of its lateral displacement y. A second change, considering this particular modal mass case of $\mu = 3$t, is the disappearence of the first stable region from the lateral branch. This means that the bistable region disappears as well and, consequently, the multiple-frequency branch now connects the lateral brach with the torsional branch instead of connecting the same lateral branch. Also, the torus bifurcation T_t on the torsional branch moved to a higher velocity in Figure 7 whereas the second Hopf bifurcation H_l moved to a lower velocity. These changes have a dual effect on the dynamics.

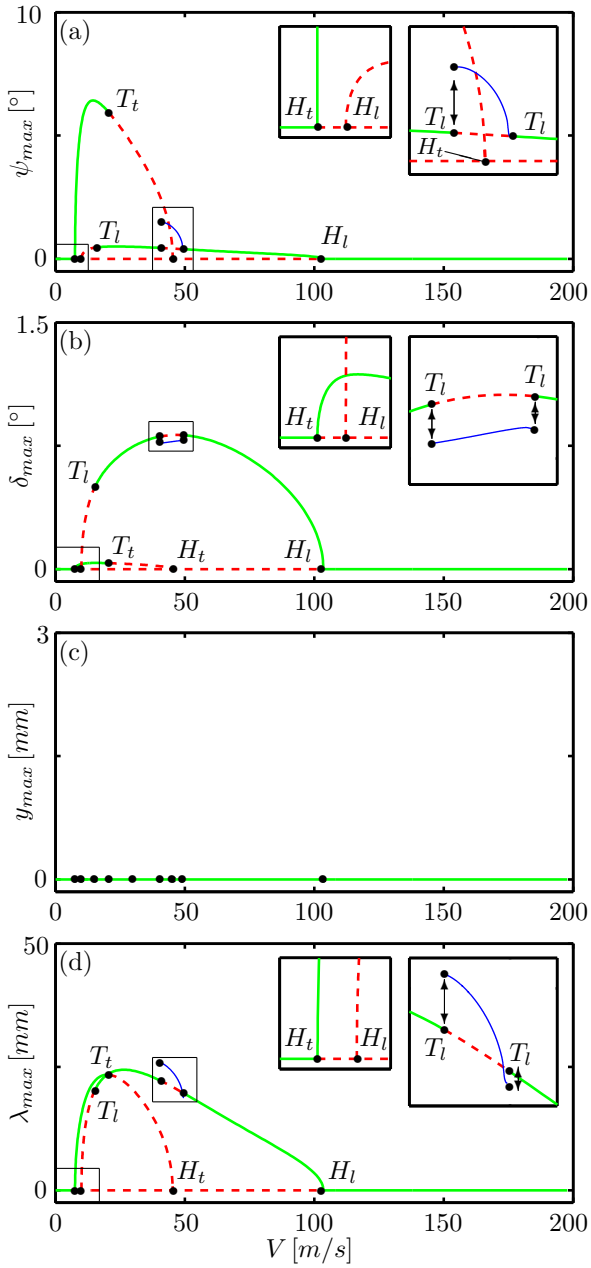

Figure 11: One-parameter bifurcation diagrams for $\mu = 15000$t and $M = 8$t. The large μ value represents an inactive modal mass. Panels (a)-(d) show the maximum amplitude of the solution for δ, ψ, y and λ, respectively, plotted as a function of V. Solid and dashed lines represent stable and unstable solutons, respectively. Arrows denote very steep unstable multiple-frequency branches.

The first is that between $V \approx 20.6$m/s and $V \approx 40.3$m/s, where the only stable solution is the lateral solution in the inactive case, the stable solutions are now either the torisonal solution ($V \approx 20.6 - 30.6$m/s) or the multiple-frequency solution ($V \approx 30.6 - 40.3$m/s); hence, in this region the lateral shimmy oscillations are now changed to torsional shimmy oscillations or multiple-frequency oscillations. Moreover, due to the relocation of the Hopf bifurcation H_l, the region where the straight-rolling solution is stable is smaller.

The differences between the one-parameter bifurcation diagrams, Figure 7 and Figure 11, can be explained by the two-parameter bifurcation diagram of Figure 10c. All are for the case $M = 8$t and the one-parameter bifurcation diagrams are horizontal slices of the two-parameter bifurcation diagram. The $\mu = 15000$t case is well out of the range of Figure 10c, but it is effectively approximated as the highest available mass load value of $\mu = 20$t, because the locations of the curves do not change significantly above that value of μ; see also Figure 9e and Figure 9f. As can be seen in Figure 10c, the reason for the loss of stability of the torsional branch occuring at a higher velocity is that the torus bifurcation curve T_t moves towards higher velocities. Also, the lack of the stable lateral solution in Figure 7 between $V \approx 15.2 - 40.3$m/s is due to the fact, that the loop of the torus bifurcation curve T_l, which bounds a region of stable lateral solutions, has a minimum at $\mu \approx 7.4$t. The loops of torus bifurcation curves T_t and T_l, therefore, are of great importance as – for a fixed value of mass load – they define limit values of modal mass μ, where the existence of stable solutions changes. The comparison of Figures 7 and 11 clearly reveals that the laterally active mass can have a significant influence on the system dynamics – depending on its modal properties and the value of the load.

IV. Conclusions

Based on an established NLG model, an extended NLG-fuselage model was presented to model the interaction between those two sub-systems. The NLG model has two degrees of freedom: the torsion angle ψ and the lateral bending angle δ, and takes into account the general three-dimensional motion that the NLG is exposed to while moving on the runway. The fuselage is modelled by a linear second-order mass-spring-damper system with one lateral degree-of-freedom y. Consequently, fuselage modes with lateral component were considered here. This fuselage model – as well as the landing gear model – is fully parametrized, and so the modal characteristics of the considered mode can be changed. The tyre is modelled by the exact stretched string model. Although the overall model is capable of handling changes in all the parameters, we focused here on changes in three of them: the forward velocity V, the vertical mass load M, and the modal mass μ of the fuselage. In terms of the fuselage model it means that the natural frequency is set to a fixed value, and the modal properties

are varied by changing the value of the modal mass μ only.

The main question of the study was at what modal mass values the landing gear can excite the considered fuselage mode and, moreover, when this interaction is significant. To this end, numerical bifurcation analysis was used and one- and two-parameter bifurcation diagrams were presented to demonstrate how the system behaviour depends on the chosen parameters. It was found, that, due to the strong coupling between the sub-systems, the landing gear can trigger vibrations in the fuselage. The amplitude and frequency of those oscillations strongly depend on the modal mass of the fuselage. This means that, given the right parameters, fuselage modes having lateral components can be excited during take-off and landing. Moreover, it was shown that a significant proportion of the excitation energy feeds modes of lower modal masses. By comparing a laterally inactive mass to an oscillating one, it was demonstrated that the fuselgage dynamics and its coupling to the landing gear have an influence on the landing gear dynamics; therefore, the extended model can improve predictions of shimmy oscillations in aircrafts.

Overall, it was shown that the model presented here is sufficient for demonstrating that significant interaction is possible between the nose landing gear and a lateral fuselage mode as represented by a mass-spring-damper system. In particular, a real-time dynamic sub-structuring test appears to be feasible. The next step towards implementing such a hybrid test would be to introduce the dynamics of the actuators and to identify control parameters at which the system is stable. The NLG-fuselage model presented considers a linear, one degree-of-freedom model of a simple fuselage mode. Moreover, the fuselage characterics were changed with the modal mass, while the natural frequency was kept fixed. A next step would be to vary the natural frequency as well. The model could also be refined with the inclusion of additional terms, such as those describing the gyroscopic effect of the wheel. A longer term goal would be a full study of the dynamic effects of an aircraft fuselage, as it is connected to the ground via the nose landing gear as well as the main landing gears; such work would require considerable further extensions of the present model.

Acknowledgement: The authors thank Sanjiv Sharma, Etienne Coetzee, Phanikrishna Thota and Peter Hart (Airbus in the UK) for helpful discussions and their support. The research of Nándor Terkovics was supported by the Engineering and Physical Sciences Research Council (EPSRC) in collaboration with Airbus in the UK.

References

[1]B. von Schlippe and R. Dietrich. Shimmying of a pneumatic wheel. Technical Report NACA TM 1365, National Advisory Committee for Aeronautics, 1947.

[2]Hans B. Pacejka. *The wheel shimmy phenomenon: a theoretical and experimental investigation with particular reference to the nonlinear problem.* Phd thesis, Delft University of Technology, 1966.

[3]Hans B. Pacejka. Analysis of the shimmy phenomenon. In *Proceedings of the Institution of Mechanical Engineers*, volume 180.1, pages 251–268, 1965.

[4]Hans B. Pacejka. *Tyre and Vehicle Dynamics.* Butterworth-Heinemann, second edition, 2006.

[5]L. Segel. Force and moment response of pneumatic tires to lateral motion inputs. *ASME, Transactions, Journal of Engineering for Industry*, 88:37–44, 1966.

[6]G. Stépán. Delay, nonlinear oscillations and shimmying wheels. In *New applications of nonlinear and chaotic dynamics in mechanics*, pages 373–386. Kluwer Academic Publisher, 1999.

[7]D. Takács, G. Orosz, and G. Stépán. Delay effects in shimmy dynamics of wheels with stretched string-like tyres. *European Journal of Mechanics A/Solid*, 28:516–525, 2009.

[8]D. Takács and G. Stépán. Experiments on quasiperiodic wheel shimmy. *Journal of Computational and Nonlinear Dynamics*, 4:031007–1, 2009.

[9]R. F. Smiley. Correlation, evaluation, and extension of linearized theories for tyre motion and wheel shimmy. Technical Report 1299, National Advisory Committee for Aeronautics, 1957.

[10]G. Somieski. Shimmy analysis of a simple aircraft nose landing gear model using different mathematical methods. *Aerospace Science and Technology*, 1(8):545–555, 1997.

[11]P. Thota, B. Krauskopf, and M. Lowenberg. Shimmy in a non-linear model of an aircraft nose landing gear with nonzerorake angle. In *Proceedings of ENOC*, 2008.

[12]P. Thota, B. Krauskopf, and M. Lowenberg. Interaction of torsion and lateral bending in aircraft nose landing gear shimmy. *Nonlinear Dynamics*, 57(3), 2009.

[13]O.S. Bursi and D.J. Wagg. Real-time testing with dynamic substructuring. In *Modern Testing Techniques for Structural Systems*, pages 293–342. Springer, 2008.

[14]A. Blakeborough, M. S. Williams, A. P. Darby, and D. M. Williams. The development of real-time substructure testing. *Philosophical Transactions of the Royal Society of London A*, 359:1869–1891, 2001.

[15]E. J Doedel, H. B Keller, and J. P Kernevez. Numerical analysis and control of bifurcation problems, part ii: bifurcation in infinite dimensions. *Int J Bifurcat Chaos Appl Sci Eng*, 1(4):745–772, 1991.

[16]P. Thota, B. Krauskopf, and M. Lowenberg. Multi-parameter bifurcation study of shimmy oscillations in a dual-wheel aircraft nose landing gear. *Nonlinear Dynamics*, 70(2):1675–1688, 2012.

[17]Yuri A. Kuznetsov. *Elements of Applied Bifurcation Theory.* Springer, 1995.

[18]P. Thota, B. Krauskopf, and M. Lowenberg. Multi-parameter bifurcation study of shimmy oscillation in a dual-wheel aircraft nose landing gear. *Nonlinear Dynamics*, 70(2):1675–1688, 2012.

[19]H. Erzgräber, B. Krauskopf, and D. Lenstra. Bifurcation analysis of a semiconductor laser with filtered optical feedback. *SIAM Journal on Applied Dynamical Systems*, 6.1:1–28, 2007.